photonics

MDPI

Communication

High-Gain AlInAsSb SACM Avalanche Photodiode for SWIR Detection at Room Temperature

Ming Liu [1,2,3,†], Shupei Jin [2,3,†], Dongliang Zhang [2,3,*], Songlin Yu [2,3], Mingxin Yao [1], Xiaoning Guan [1], Feng Zhou [1] and Pengfei Lu [1,*]

[1] School of Integrated Circuits, Beijing University of Posts and Telecommunications, Beijing 100015, China
[2] North China Research Institute of Electro-Optics, Beijing 100015, China
[3] National Key Laboratory of Infrared Detection Technologies, Beijing 100015, China
* Correspondence: zdllzu2007@163.com (D.Z.); lupengfei@bupt.edu.cn (P.L.)
† These authors contributed equally to this work.

Abstract

We report the design, epitaxial growth, and room-temperature operation of a high-gain AlInAsSb-based avalanche photodiode (APD) for short-wavelength infrared (SWIR) detection at 1.55 μm. The device employs SAGCM structure to confine the electric field within the multiplication region while suppressing dark current. High-quality AlInAsSb layers were grown on GaSb substrates by molecular beam epitaxy using a digital alloy approach, achieving excellent surface morphology (R_a < 0.2 nm) and uniform superlattice periodicity. Electrical characterization reveals a well-defined breakdown voltage near −17 V and a peak internal multiplication gain of 200 at 300 K under 0.2 mW illumination at 1550 nm—among the highest gains reported to date for antimonide-based APDs operating at room temperature. Variable-temperature dark current analysis indicates a transition from tunneling-dominated to thermally generated dark current as temperature increases from 100 K to 300 K. These results demonstrate the strong potential of AlInAsSb SAGCM APDs for eye-safe, high-sensitivity applications in LIDAR, free-space optical communication, and low-light SWIR imaging.

Keywords: AlInAsSb; avalanche photodiode (APD); room temperature

1. Introduction

Short-wavelength infrared (SWIR) radiation, spanning 1.5–3 μm, has found widespread application in low-light imaging, precision guidance, space-based remote sensing, near-infrared spectroscopy, industrial control, biomedical diagnostics, and aerospace systems. A key advantage of SWIR imaging stems from its reliance on reflected ambient light, such as sunlight, moonlight, and starlight, enabling robust target recognition even under minimal illumination [1–4]. However, the increasing deployment of laser imaging, detection, and ranging (LIDAR) systems in high-density urban environments demands higher laser power to extend detection range and improve sensitivity, thereby raising concerns about ocular safety. The use of longer-wavelength lasers offers a compelling solution: the ~2 μm spectral band lies within an atmospheric transmission window, supports long-range propagation, and is classified as "eye-safe" due to strong absorption in the cornea and aqueous humor before reaching the retina [5]. Consequently, high-gain SWIR avalanche photodiodes (APDs) operating near 2 μm represent an ideal platform for next-generation LIDAR in autonomous and defense applications where photon-starved conditions demand

Check for updates

Received: 12 March 2026
Revised: 1 April 2026
Accepted: 8 April 2026
Published: 14 April 2026

Copyright: © 2026 by the authors. Licensee MDPI, Basel, Switzerland. This article is an open access article distributed under the terms and conditions of the Creative Commons Attribution (CC BY) license.

gain >100 and low excess noise. Over decades, high-performance APDs have been realized using various semiconductors, including GaN, GaAs, InGaAs, InGaAsP, and HgCdTe [6]. More recently, antimonide-based type-II superlattices (T2SLs) comprising InAs, GaSb, AlSb, and their quaternary alloys have emerged as a versatile material platform, offering precise bandgap engineering and the potential for low-noise avalanche multiplication through selective control of electron and hole ionization coefficients by designing the multiplication material structure.

Despite these advances, achieving high avalanche gain at room temperature remains a significant challenge for antimonide-based APDs due to the inherently small band offsets and strong temperature-dependent dark currents. To date, most reported InAs/GaSb type-II superlattice (T2SL) APDs exhibit substantial gain only at cryogenic temperatures (<200 K). For instance, the 2007 Illinois device achieved a gain of 580—but only at 77 K [7]. Even recent MWIR T2SL APDs from Northwestern University (2022) [8] and the Chinese Academy of Sciences (2021) [9] demonstrated gains of only 29 and 6.1, respectively, at 200 K, with negligible or unreported room-temperature multiplication. The AlInAsSb material system offers improved prospects due to its larger conduction-band offset and lower ionization coefficient ratio (k~0.01) [10–13]. The 2020 Nature Photonics report by Virginia/Texas achieved a gain of 100 at room temperature in a 2 μm separate absorption, charge, and multiplication (SACM) APD, representing a major milestone [12]. However, few subsequent studies have surpassed this gain benchmark under practical operating conditions. As summarized in Table 1 (see below), no previously reported AlInAsSb or T2SL APD has simultaneously demonstrated a room-temperature gain exceeding 100 and operation at standard eye-safe wavelengths (e.g., 1.55 μm). This performance gap underscores the need for optimized heterostructure design, high-quality epitaxy, and effective dark current suppression strategies, which are challenges that the present work directly addresses. High-gain, room-temperature SWIR APDs are critical enablers for compact, low-SWaP (size, weight, and power) LIDAR systems in UAVs and space platforms. Thus, we report herein the design and fabrication of a high-gain AlInAsSb-based APD that achieves a multiplication gain of 200 at room temperature.

Table 1. Comparison of Material Systems and Max Gain in MWIR/SWIR APDs.

Reference	Material System	λ (μm)	Temp. (K)	Max Gain	Structure
[7]	InAs/GaSb T2SL	MWIR	77	580	SAM
[8]	AlAsSb/GaSb T2SL	MWIR	200	29	SAM
[9]	InAs/GaSb/AlAsSb	MWIR	200	6.1	SACM
[12]	AlInAsSb	2.0	300	100	SACM
This work	AlInAsSb	SWIR	300	200	SAGCM

2. Materials and Methods

To realize a high-gain APD operable at room temperature, we adopted a separate absorption, grading, charge, and multiplication (SAGCM) architecture [14,15]. This design spatially isolates the absorption, charge, and multiplication regions to engineer the internal electric field profile. Furthermore, a compositionally graded layer was inserted between the multiplication and absorption regions to suppress dark current and enhance avalanche gain. The resulting device structure is illustrated in Figure 1. The conduction band and valence band profiles, as well as the electric field distribution under operational bias at 300 K, were simulated by Nuwa TCAD (V2024, GMPT Company, Ltd., Shanghai, China) and the results are presented in Figures 2 and 3, respectively. Owing to the use of wide-bandgap AlInAsSb in the lower contact layer, the bandgap begins to widen at a depth of 0.65 μm. Avalanche multiplication occurs within the 1.2–1.7 μm multiplication layer, where the electric field

peaks. Beyond 1.72 µm, the bandgap gradually narrows due to the presence of the graded transition layer, enabling a smooth band alignment with the narrow-gap absorption region. As confirmed by electric field simulations, this heterostructure establishes a localized high-field region exclusively within the multiplication layer confined by the adjacent charge control and graded layers, while maintaining a low electric field in the absorption region. This ensures efficient carrier collection without premature drift-induced recombination, thereby enabling robust device operation.

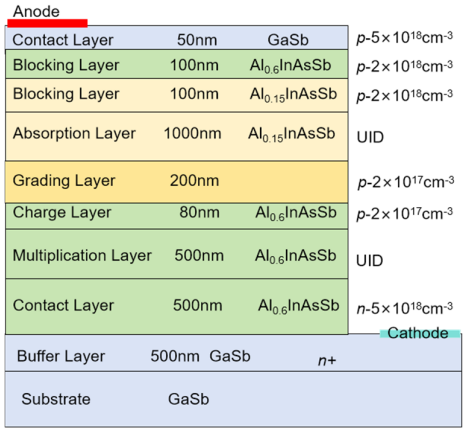


Figure 1. The structure of AlInAsSb APD.

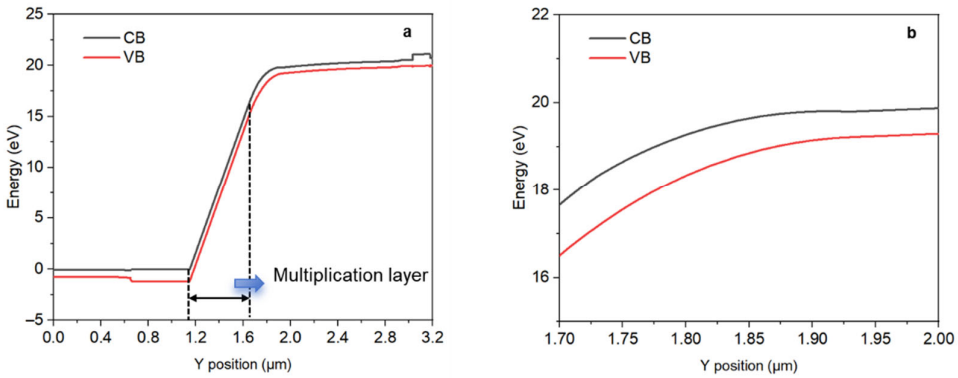


Figure 2. Energy band diagram under −20 bias: (**a**) complete energy band; (**b**) local band structure.

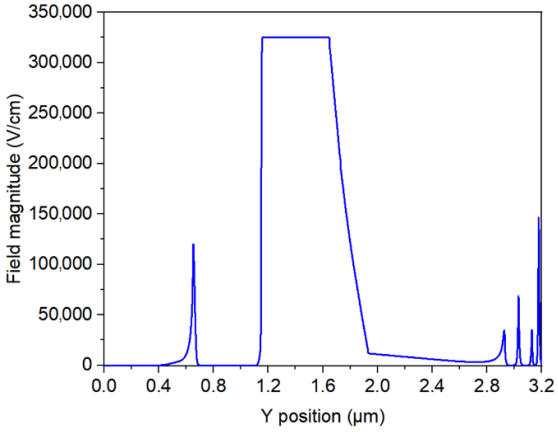


Figure 3. Electric field diagram under −20 bias.

Based on these design principles, the full epitaxial structure was grown on a 2-inch GaSb (100) substrate by solid-source molecular beam epitaxy (MBE) [16] using a DCA

N850 system (DCA Instruments Oy, Turku, Finland). To achieve high-quality quaternary AlInAsSb alloys, which are challenging to grow directly due to phase separation and stoichiometric complexity, we employed a digital alloy approach [17–20]. This technique synthesizes an effective quaternary compound by periodically stacking ultrathin layers of binary constituents, leveraging superlattice averaging to emulate the desired bulk properties [18]. Specifically, four fundamental binaries, i.e., AlAs, AlSb, InAs, and InSb, were used as elemental building blocks. To minimize group-V intermixing and enhance interface sharpness, adjacent layers were designed to share at least one common atomic species. Moreover, because AlAs and InSb exhibited a large lattice mismatch (~7%) on GaSb, they were restricted to ultrathin interfacial layers rather than extended growth segments. Consequently, each digital alloy cycle followed the same sequence: AlAs/AlSb/InAs/InSb, with multiple repetitions to achieve the target average composition.

The structural quality of the as-grown epitaxial wafer was evaluated across multiple sites. Surface defect density was assessed using optical microscopy over a defined test field measuring 344 μm × 245 μm (area = 0.08428 cm^2), as shown in Figure 4. The measured defect density was consistently below 120 cm^{-2}, indicating excellent surface integrity. Atomic force microscopy (AFM) was performed over a 5 μm × 5 μm scan area (Figure 5), revealing well-defined atomic steps, a root-mean-square surface roughness (R_a) of less than 0.2 nm, and minimal topographic undulation—hallmarks of high surface crystallinity. Additionally, high-resolution X-ray diffraction (XRD) rocking curves (Figure 6) exhibited pronounced zeroth-order satellite peaks with angular positions varying by less than 200 arcsec across the wafer, confirming uniform superlattice periodicity and low strain accumulation. Collectively, these characterizations, namely, surface morphology, roughness, and XRD, demonstrate that the epitaxially grown AlInAsSb heterostructure possesses excellent crystal quality and compositional homogeneity, fulfilling the stringent requirements for high-performance APD fabrication.

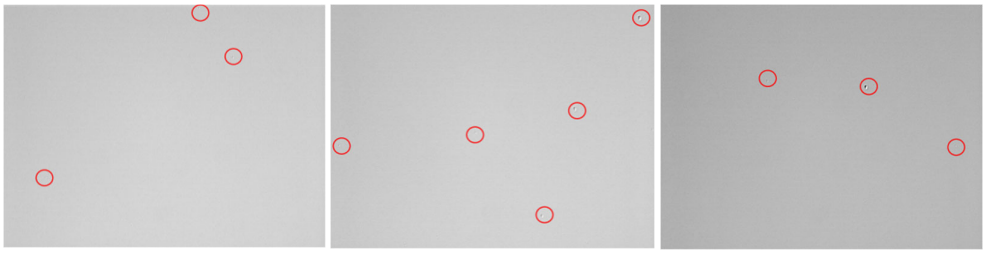


Figure 4. Surface defect density diagram.

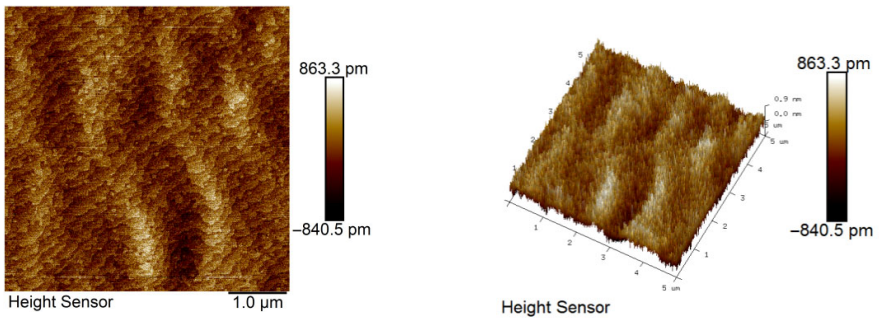


Figure 5. Atomic force microscopy characterization results.

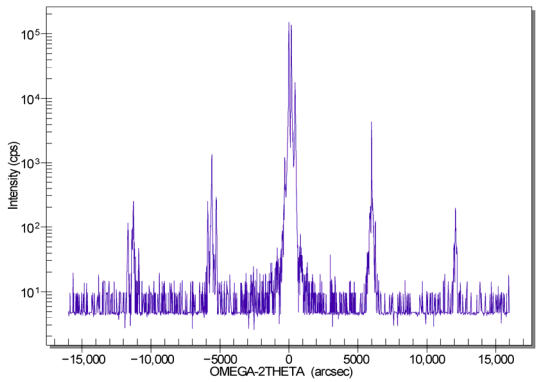


Figure 6. X-ray diffraction test results.

3. Results and Discussion

The devices reported in this work are single-element mesa-type APDs. Starting from the MBE-grown AlInAsSb heterostructure, pixel isolation was achieved by defining mesas via photolithography followed by selective wet chemical etching. A SiO_xN_γ/SiO_2 bilayer passivation stack was then deposited conformally over the mesa sidewalls and top surface using plasma-enhanced chemical vapor deposition (PECVD). Contact vias were subsequently opened through the passivation layer by reactive ion etching. Ti/Pt/Au metal contacts were formed on both the top n-type and bottom p-type layers using electron-beam evaporation and lift-off lithography, completing the device fabrication process. Circular mesas with diameters of 50 μm, 100 μm, 150 μm, 200 μm, and 300 μm were fabricated; the optical micrographs of representative devices are shown in Figure 7. All completed devices underwent comprehensive electrical and optoelectronic characterization.

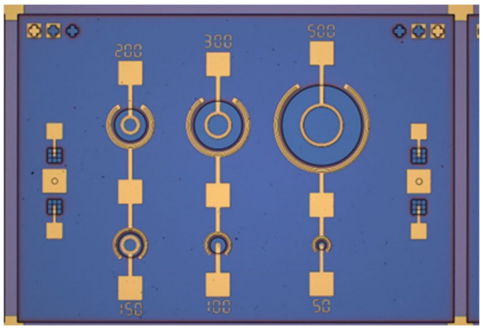


Figure 7. Microscopic image of the surface of the unit device.

The electrical performance of antimonide-based SWIR APDs was evaluated through current–voltage (I–V) measurements under both dark and illuminated conditions, yielding the dark current (I_{dark}) and total photocurrent (I_{total}), respectively. In general, I_{dark} arises from several mechanisms, including minority carrier diffusion, generation recombination (G-R) current related to bulk defects and trap states, electric field-assisted tunneling, and surface leakage. The G-R contribution is typically associated with Shockley-Read-Hall (SRH) processes, while the tunneling current may include trap-assisted tunneling (TAT) and band-to-band tunneling in high-field regions [21]. For mesa devices, surface leakage can be further aggravated by rough sidewalls, incomplete passivation, or plasma-induced etching damage. Importantly, in APDs, these dark current components can be further amplified by avalanche multiplication in the high field multiplication region, making the dark current a dominant noise source.

To identify the dominant dark current mechanisms across temperature, variable-temperature I–V measurements were performed from 100 K to 300 K in 50 K steps. Devices

were mounted in a liquid-nitrogen-cooled Dewar and tested. A calibrated diode integrated provided accurate temperature monitoring via voltage readout. A 500 μm diameter device was selected for these tests, and the resulting dark current density is plotted in Figure 8.

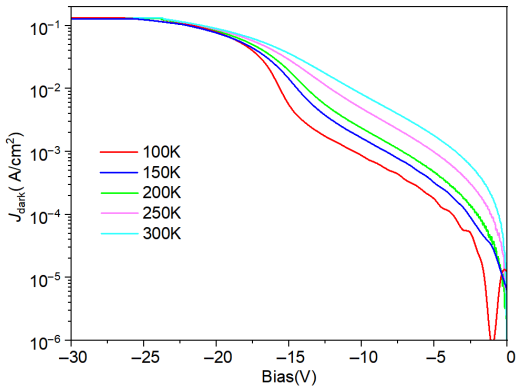


Figure 8. Temperature-variable dark current density under 0~−30 V bias voltage.

As shown, the dark current density remains low at small reverse biases (<−10 V), likely dominated by surface leakage or diffusion processes. With increasing bias, the current rises gradually and then exhibits a sharp increase near −16 V, suggesting the onset of avalanche multiplication. At higher biases (e.g., −22 V), the dark current saturates in its rate of increase, consistent with full avalanche gain where the primary dark current components are internally amplified. Notably, the characteristic "kink" or inflection point associated with the onset of gain becomes less pronounced at elevated temperatures. This behavior is attributed to the growing contribution of thermally generated carriers at higher temperatures, which masks the relatively weaker, temperature-insensitive tunneling component dominant at cryogenic conditions. Additionally, parasitic noise from long bond wires in the Dewar setup may contribute to measurement uncertainty at room temperature. It should be noted that the slight shift in the current minimum toward a bias below 0 V at 100 K is most likely caused by a small residual voltage offset in the cryogenic Dewar measurement loop, rather than by a change in the intrinsic dark current mechanism. At higher temperatures, the thermally activated dark current is much larger, so this small offset becomes negligible and no obvious shift is observed.

To minimize ambient and setup-induced noise, complementary room-temperature I–V measurements were conducted directly on a probe station. Under 1550 nm illumination (optical power = 0.2 mW), the total output current includes both the primary light current and its avalanche-amplified component. The effective multiplication gain (M) is defined as:

$$M = \frac{I_{total} - I_{dark}}{I_{light,0}}$$

where $I_{light,0} = I_{total,0} - I_{dark,0}$, which represents the primary photocurrent at zero gain (i.e., below breakdown). Figure 9 presents the dark current, light current, and extracted gain for devices with mesa diameters of 200 μm, 300 μm, and 500 μm under maximum reverse bias up to −30 V. The results confirm clear avalanche gain characteristics at 300 K, validating the efficacy of the SAGCM design. No distinct gain "knee" is observed in the dark current, consistent with thermal generation dominating the dark current at room temperature—as also inferred from the variable-temperature study. The dark current scales approximately with device area: at −30 V, it is below 10^{-5} A for the 200 μm device, ~10^{-5} A for 300 μm, and approaches 10^{-4} A for 500 μm. At the same time, the relatively high area-normalized dark current indicates that surface leakage remains non-negligible. In particular, the 200 μm device exhibits a relatively higher minimum dark current, which

is likely related to its larger perimeter-to-area ratio, making the device more sensitive to sidewall damage, surface states, imperfect passivation, and local electric field enhancement near the mesa edges. The bias corresponding to the minimum dark current also does not vary monotonically with mesa size, suggesting that the minimum dark current point is determined by the competition between bulk dark current and surface leakage components rather than by mesa size alone. For the 300 μm device, these two contributions are likely of comparable magnitude, making the minimum more sensitive to local sidewall conditions, defect distribution, and process variation. These results indicate that further optimization of passivation and mesa etching is required to suppress edge-related leakage.

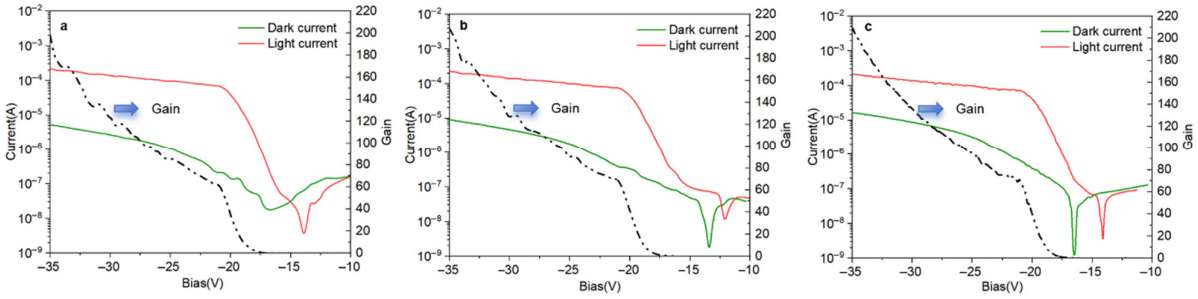


Figure 9. Dark current, light current, and extracted gain for devices with different mesa diameters: (**a**) 200 μm; (**b**) 300 μm and (**c**) 500 μm; the red curve corresponds to the net light current, rather than the total illuminated current.

The light current obtained by subtracting I_{dark} from I_{total} remains nearly flat between −14 V and −17 V, indicating negligible internal gain in this bias range. The breakdown voltage (V_{br}) is estimated to be approximately −17 V. Beyond this point, the light current increases rapidly due to impact ionization, signaling the onset of avalanche multiplication. Although the test setup limited biasing beyond −30 V (preventing full observation of breakdown dynamics), a peak multiplication gain of 200 was achieved at room temperature—among the highest reported for AlInAsSb-based APDs to date.

To further clarify the origin of the dark current, the dark current density was calculated (Table 2) and analyzed as a function of the perimeter-to-area ratio P/A for mesas with different diameters when the bias voltage is approximately −17 V. As shown in Figure 10, J_{dark} increases monotonically with increasing P/A and can be approximately described by a linear fit. This behavior is consistent with the standard model:

$$J_{total} = \frac{P}{A} J_{surface} + J_{bulk}$$

where J_{bulk} denotes the bulk-related dark current density and $J_{surface}$ represents the surface leakage contribution. The positive slope confirms that surface leakage is significant. Therefore, the total dark current in the present APDs is governed by both bulk dark current and surface dark current contributions, and the latter becomes increasingly important for smaller mesas with larger P/A. This result is consistent with the relatively higher minimum dark current observed in the smaller devices and suggests that further optimization of mesa etching and sidewall passivation is still required.

Table 2. Dark current density for devices with different mesa diameters.

D (μm)	P (cm)	A (cm^2)	P/A	J_{dark} (A/cm^{-2})
200	0.1257	0.0012566	100	1.7608×10^{-4}
300	0.1885	0.002827	66.67	1.4228×10^{-4}
500	0.3142	0.007854	40	1.134×10^{-4}

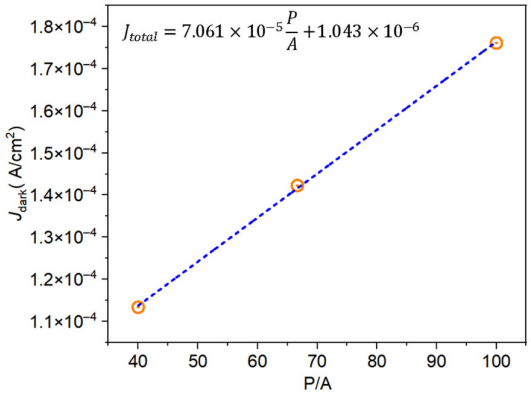


Figure 10. Dark current density J_{dark} as a function of perimeter-to-area ratio P/A for APDs with different mesa diameters at −17 bias.

4. Conclusions

In this work, we have designed and demonstrated a high-gain AlInAsSb heterojunction avalanche photodiode (APD) based on an SAGCM architecture. Band structure and electric field simulations at 300 K confirm that the proposed device effectively confines the high electric field to the multiplication region while ensuring a gradual field reduction across the graded transition layer into the low-field absorption region—thereby enabling efficient carrier collection and controlled avalanche gain.

High-quality AlInAsSb epitaxial layers were grown on GaSb substrates by molecular beam epitaxy, exhibiting excellent crystallinity, low surface roughness (<0.2 nm), and uniform superlattice periodicity, as verified by AFM and XRD. Mesa-type unit devices with varying diameters were fabricated and characterized. Variable-temperature dark current measurements (100–300 K) revealed a clear transition in the dominant dark current mechanism: from tunneling-dominated transport at cryogenic temperatures to thermally generated diffusion current at room temperature. This shift explains the diminishing visibility of the gain "knee" in dark I–V curves as temperature increases.

Under 1550 nm illumination (0.2 mW optical power) at room temperature, the device exhibited a well-defined breakdown voltage near −17 V and achieved a peak internal multiplication gain of 200—among the highest reported for antimonide-based SWIR APDs operating at 300 K. These results validate the effectiveness of the SAGCM design combined with compositionally graded AlInAsSb layers in enabling high-sensitivity, eye-safe photodetection for next-generation LIDAR and free-space optical communication systems.

Author Contributions: Conceptualization, M.L.; methodology, S.J.; software, D.Z.; validation, S.Y., F.Z. and M.Y.; formal analysis, X.G.; investigation, M.L.; resources, P.L.; data curation, D.Z.; writing—original draft preparation, M.L.; writing—review and editing, M.L., D.Z. and P.L.; funding acquisition, P.L. All authors have read and agreed to the published version of the manuscript.

Funding: This research was funded by the Open Project of the National Key Laboratory of Infrared Detection, grant number No. IRDT-24-02.

Institutional Review Board Statement: Not applicable.

Informed Consent Statement: Informed consent was obtained from all subjects involved in the study.

Data Availability Statement: Data are contained within the article.

Conflicts of Interest: The authors declare no conflicts of interest.

References

1. MacDougal, M.; Hood, A.; Geske, J.; Wang, J.; Patel, F.; Follman, D.; Manzo, J.; Getty, J. InGaAs focal plane arrays for low-light-level SWIR imaging. In Proceedings of the Infrared Technology and Applications XXXVII, Orlando, FL, USA, 25–29 April 2011.
2. Battaglia, J.; Blessinger, M.; Enriquez, M.; Ettenberg, M.; Evans, M.; Flynn, K.; Lin, M.; Passe, J.; Stern, M.; Sudol, T. An uncooled 1280 × 1024 InGaAs focal plane array for small platform, shortwave infrared imaging. *Proc. SPIE* **2010**, *7298*, 72983C.1–72983C.8.
3. Richards, A.A. Emerging applications for high-performance near-infrared imagers. In Proceedings of the Thermosense XXIV, Orlando, FL, USA, 1–5 April 2002.
4. Ma, X.; Li, Y.; Huang, R.; Ye, H.; Hou, Z.; Shi, Y. Development and applications of short-wave infrared detectors (Invited). *Infrared Laser Eng.* **2022**, *51*, 135–146.
5. Campbell, J.C. Recent Advances in Avalanche Photodiodes. *J. Light. Technol.* **2016**, *34*, 278–285. [CrossRef]
6. Rogalski, A.; Antoszewski, J.; Faraone, L. Third-generation infrared photodetector arrays. *J. Appl. Phys.* **2009**, *105*, 091101. [CrossRef]
7. Mallick, S.; Banerjee, K.; Ghosh, S.; Rodriguez, J.B.; Krishna, S. Midwavelength Infrared Avalanche Photodiode Using InAs–GaSb Strain Layer Superlattice. *IEEE Photonics Technol. Lett.* **2007**, *19*, 1843–1845. [CrossRef]
8. Li, J.; Dehzangi, A.; Brown, G.; Razeghi, M. Mid-wavelength infrared avalanche photodetector with AlAsSb/GaSb superlattice. *Sci. Rep.* **2021**, *11*, 7104. [CrossRef] [PubMed]
9. Yan, S.; Huang, J.; Zhang, Y.; Ma, W. Mid Wavelength Type II InAs/GaSb Superlattice Avalanche Photodiode with AlAsSb Multiplication Layer. *IEEE Electron Device Lett.* **2021**, *42*, 1634–1637. [CrossRef]
10. Woodson, M.E.; Ren, M.; Maddox, S.J.; Chen, Y.; Bank, S.R.; Campbell, J.C. Low-noise AlInAsSb avalanche photodiode. *Appl. Phys. Lett.* **2016**, *108*, 081102. [CrossRef]
11. Bank, S.R.; Campbell, J.C.; Maddox, S.J.; Ren, M.; Rockwell, A.K.; Woodson, M.E.; March, S.D. Avalanche Photodiodes Based on the AlInAsSb Materials System. *IEEE J. Sel. Top. Quantum Electron.* **2018**, *24*, 1–7. [CrossRef]
12. Jones, A.H.; March, S.D.; Bank, S.R.; Campbell, J.C. Low-noise high-temperature AlInAsSb/GaSb avalanche photodiodes for 2-µm applications. *Nat. Photonics* **2020**, *14*, 559–563. [CrossRef]
13. McArthur, J.A.; Dadey, A.A.; March, S.D.; Jones, A.H.; Xue, X.; Salas, R.; Campbell, J.C.; Bank, S.R. Demonstration of the AlInAsSb cascaded multiplier avalanche photodiode. *Appl. Phys. Lett.* **2023**, *123*, 041106. [CrossRef]
14. Xiao, Y.G.; Lestrade, M.; Li, Z.Q.; Li, Z.M.S. Modeling of AlInAsSb waveguide avalanche photodiodes for MWIR applications. *J. Instrum.* **2025**, *20*, C04005. [CrossRef]
15. Guo, Y.; Yu, J.; Chen, W.; Zhu, L.; Lu, L. Multi-step Multiplication Structure with Low Excess Noise for the AlInAsSb Avalanche Photodiode. *J. Electron. Mater.* **2024**, *53*, 8078–8086. [CrossRef]
16. Maddox, S.J. High-Gain, Low-Noise Avalanche Photodiodes Grown by Molecular Beam Epitaxy. Doctoral Dissertation, University of Texas Austin, Austin, TX, USA, 2015.
17. Zheng, D.-N.; Su, X.-B.; Xu, Y.-Q.; Niu, Z.-C. High gain and low dark current AlInAsSb avalanche photodiodes grown by quaternary digital alloys. *J. Infrared Millim. Waves* **2021**, *40*, 172.
18. Lyu, Y.; Han, X.; Sun, Y.; Jiang, Z.; Guo, C.; Xiang, W.; Dong, Y.; Cui, J.; Yao, Y.; Jiang, D.; et al. Digitally grown AlInAsSb for high gain separate absorption, grading, charge, and multiplication avalanche photodiodes. *J. Cryst. Growth* **2018**, *482*, 70–74. [CrossRef]
19. Zhang, N.; Jones, A.H.; Deng, Z.; Chen, B. Defect characterization of AlInAsSb digital alloy avalanche photodetectors with low frequency noise spectroscopy. *Opt. Express* **2020**, *28*, 11682–11691. [CrossRef] [PubMed]
20. Zhou, W.; Liang, Y.; Li, N.; Chang, F.; Jiang, J.; Chen, W.; Jiang, D.; Hao, H.; Wu, D.; Wang, G.; et al. High responsivity short-wavelength dual-band photodetector based on AlInAsSb digital alloy. *Infrared Phys. Technol.* **2023**, *133*, 104763. [CrossRef]
21. Ghosh, S.; Sun, G.; Morgan, T.A.; Forcherio, G.T.; Cheng, H.H.; Chang, G.E. Dark Current Analysis on GeSn p-i-n Photodetectors. *Sensors* **2023**, *23*, 7531. [CrossRef] [PubMed]

Disclaimer/Publisher's Note: The statements, opinions and data contained in all publications are solely those of the individual author(s) and contributor(s) and not of MDPI and/or the editor(s). MDPI and/or the editor(s) disclaim responsibility for any injury to people or property resulting from any ideas, methods, instructions or products referred to in the content.